OPEN ACCESS
IOP Publishing | Songshan Lake Materials Laboratory
Materials Futures
Mater. Futures 1 (2022) 045102 (9pp)
https://doi.org/10.1088/2752-5724/ac9cf7

Facile molten salt synthesis of carbon-anchored TiN nanoparticles for durable high-rate lithium-ion battery anodes

Ruijia Liu[1,2], Na Li[3], Enyue Zhao[3,*], Jinkui Zhao[3,4], Lingxu Yang[3], Wenjun Wang[3], Huijun Liu[3,*] and Chaoliu Zeng[3,*]

[1] School of Materials Science and Engineering, University of Science and Technology of China, Shenyang 110016, People's Republic of China
[2] Institute of Metal Research, Chinese Academy of Sciences, Shenyang 110016, People's Republic of China
[3] Songshan Lake Materials Laboratory, Dongguan 523808, People's Republic of China
[4] Beijing National Laboratory for Condensed Matter Physics, Institute of Physics, Chinese Academy of Sciences, Beijing 100190, People's Republic of China

E-mail: eyzhao@sslab.org.cn, hui_jun_liu@163.com and clzeng@imr.ac.cn

Received 22 September 2022, revised 13 October 2022
Accepted for publication 23 October 2022
Published 4 November 2022

Abstract

Transition metal nitrides (TMNs), including titanium nitride (TiN), exhibit remarkable application prospects as anodes for durable high-rate lithium-ion batteries (LIBs). Regrettably, the absence of simple synthesis methods restricts their further development. Herein, a facile and low-cost molten salt synthesis strategy was proposed to prepare carbon-anchored TiN nanoparticles as an advanced anode material for LIBs with high rate capabilities. This nanosized TiN obtained is ~5 nm in size and well-distributed onto carbon plates, which could release a reversible capacity of ~381.5 mAh g^{-1} at 0.1 A g^{-1} after 250 cycles and ~141.5 mAh g^{-1} at 1.0 A g^{-1} after 1000 cycles. Furthermore, it was confirmed that the conversion reaction between TiN and Li-ions happened during the electrochemical reaction process, resulting in the formation of Li_3N and Ti. This unique microstructure attributed from TiN nanoparticles anchored by carbon could support the structural volume during cycling. This work highlights the method superiority of TiN prepared via a molten salt synthesis strategy as an anode for LIBs with impressive rate performances.

Supplementary material for this article is available online

Keywords: lithium-ion batteries, titanium nitride, anode, molten salt, nanoparticles

* Authors to whom any correspondence should be addressed.

Future perspectives
Lithium-ion batteries (LIBs) have been extensively applied in diverse ways owing to their high energy density, increased operation safety, and impressive environmental friendliness. For the future development of LIBs, research efforts should focus on the development of durable high-rate anode materials based on a simple synthesis method at a low cost. TMNs are promising candidates as high-rate anodes for LIBs due to their impressive redox capabilities, prominent electrical conductivities, and excellent chemical stability, etc. Developing the facile preparation technique of TMNs at a cheap cost may be the future direction of high-rate anode materials for LIBs. Meanwhile, the facile and low-cost molten synthesis route of nanosized TMNs would direct scalable production for advanced high-rate LIBs applications.

1. Introduction

Due to advantages of high energy density, excellent cycling stability, and environmental friendliness, rechargeable LIBs have attracted remarkable attention in energy storage fields, including electric vehicles and portable electronic devices [1–3]. However, the rapid development of fast-charging LIBs still remains challenging owing to the absence of suitable anode materials. Restricted by the low theoretical capacity (372 mAh g^{-1}) and poor high-rate capacities, commercial graphite anode cannot well satisfy the requirements of fast-charging LIBs [4]. Therefore, it is of far-reaching significance to develop and explore diverse novel anode materials for high-performance LIBs with exceptional rate properties.

For the exploration of durable high-rate LIB anodes, a variety of electrode materials involving transition metal oxides (TMOs), sulfides, MXenes, and lithium alloys has been studied extensively. Yan *et al* have prepared 3D hollow porous V_2O_5 microspheres by a one-step template-free solvothermal-based method [5]. The obtained V_2O_5 can release a capacity of 416 mAh g^{-1} after 200 cycles at a current density of 0.5 A g^{-1}. To further enhance the capacities of TMOs, carbon-coated yolk-shell V_2O_3 microspheres were synthesized via a template-free polyol solvothermal technique, and delivered a discharge capacity of 437.5 mAh g^{-1} after 100 cycles at 0.1 A g^{-1} [6]. For the transition metal sulfides, MoS_2 synthesized by a hydrothermal method could also show remarkable rate properties, with a reversible capacity of ∼300 mAh g^{-1} at 1.0 A g^{-1} after 100 cycles [7]. Meanwhile, novel two-dimensional layered MXenes were applied as high-performance anodes for LIBs. Ti_3C_2 and V_4C_3 prepared by etching Ti_3AlC_2 and V_4AlC_3 precursors in aqueous HF solutions exhibited discharge capacities of 150 mAh g^{-1} at 0.5 °C and 130.9 mAh g^{-1} at 1.0 °C, respectively [8, 9]. In terms of lithium alloys, aluminum-lithium (Al-Li) alloy is also considered as a stable and reversible anode for high-rate LIBs [10]. When coupled with $LiFePO_4$ cathode to assemble a full cell, it can release ∼154.6 mAh·g^{-1} at 0.5 °C. Although substantial endeavors have been dedicated to the exploitation of high-rate anode materials for LIBs, these aforementioned synthesis methods above have turned out to be either operation-complex or expensive, which is not suitable for mass production and commercialization. Thus, a variety of exploration still needs to be committed into other new-type anode materials for durable high-rate LIB anodes.

Impressively, transition metal nitrides (TMNs) hold great promise as high-rate anodes for LIBs owing to their high electrical conductivities, excellent chemical and thermal stability, and strong redox abilities of TM elements, which could accommodate the strain variation at large current densities [11–13]. Until now, a broad series of TMNs have been developed and studied as potential anode materials for LIBs with excellent high-rate capabilities. VN hollow spheres were fabricated by a hydrothermal method and followed with the calcination process under ammonia atmosphere [14]. These VN hollow spheres can release a reversible capacity of 400 mAh g^{-1} at 1.0 A g^{-1}. Based on a hydrothermal method followed by the annealing on a carbon fabric, Balogun *et al* have prepared nanowire-stuctured TiN [15]. A remarkable high-rate capacity of 455 mAh g^{-1} was maintained after 100 cycles at 0.335 A g^{-1} without capacity decay for these synthesized TiN nanowires. Synchronously, to further improve the rate capability, TiN was also designed or constructed with carbon materials to form high-conductivity composites. For instance, porous TiN/N-doped carbon composite was synthesized by a two-step pyrolysis of the mixture of melamine and titanium metal-organic framework under argon atmosphere [16], and showed a high-rate capacity of 281 mAh g^{-1} at 2.0 A g^{-1}. Although great progress has been made with regard to the preparation and application of TMNs as high-rate anodes for LIBs, all the preparation techniques have also appeared to be high-cost, complicated, time-consuming or high-polluting, which cannot meet the requirements of scalable syntheses well. Thus, it is urgent and imperative to explore a low-cost, facile, and efficient synthesis strategy to prepare TMNs with prominent rate properties.

Herein, we report a simple and low-cost molten salt synthesis method to prepare carbon-anchored TiN nanoparticles (TiN@C) which show excellent rate capabilities. As-obtained TiN@C could display a reversible discharge capacity of ∼381.5 mAh g^{-1} at 0.1 A g^{-1} after 250 cycles and ∼141.5 mAh g^{-1} at 1.0 A g^{-1} after 1000 cycles, respectively. *Ex-situ* x-ray diffraction (XRD), Raman, and XPS measurements were used to systematically study the electrochemical reaction kinetics and Li-ions storage mechanisms of TiN@C. This work provides novel insights for the design of TMNs as durable high-rate anodes for LIBs.

2. Experimental section

2.1. Material preparation

Carbon-anchored TiN nanoparticles (TiN@C) powders were prepared via a simple molten salt synthesis method. Ti (325 mesh, Beijing Xing Rong Yuan Technology Co., LTD) and melamine ($C_3H_6N_6$) powders (Sinopharm Chemical Reagent

Co., LTD) with a molar ratio of 1.30 were weighed and blended uniformly with eutectic (Li,K)Cl salts (Aladdin Biochemical Technology Co., Ltd) in an alumina crucible. The mass ratio between salts and raw materials was about 10:1. Then the mixture was sintered at different reaction temperatures (500 °C, 600 °C, 700 °C, 800 °C, and 900 °C) holding for 3 h under the flowing argon (Ar) atmosphere to synthesize TiN@C. After reaction, as-obtained samples were washed by deionized water to remove residual salts thoroughly. The final TiN@C powders were obtained after being dried at 120 °C overnight.

2.2. Material characterization

Field emission scanning electron microscope (Gemini 300) and high-resolution transmission electron microscopy (HRTEM, JEOL F200) coupled with selected area electron diffraction (SAED) were applied to study the morphologies and microstructures of TiN@C. The crystal structure of TiN@C was detected by XRD (Rigku miniflex 600) equipped with Cu-Kα radiation in the 2θ range of 10°–90°. Rietveld refinement of as-collected XRD data was performed using a FullProf program [17]. An energy dispersive x-ray spectrometer (EDS), Raman spectrometer (Horiba LabRam HR Evolution) with 532 nm laser, and x-ray photoelectron spectroscopy (XPS, ESCALAB XI+) coupled with a monochromated Al-Kα radiation were used to analyze the element and chemical compositions of TiN@C samples.

2.3. Electrode preparation and cell assembly

CR2025 coin-type batteries were assembled inside an Ar-filled glove box (Mikrouna) using metallic Li sheets as counter electrodes, Celgard 2325 porous polypropylene as separator, 1 mol l^{-1} $LiPF_6$ dissolved in EC/EMC/DEC (volume ratio: 1:1:1) as electrolyte, and TiN@C electrodes as working electrodes, respectively. The ratio of electrolyte to electrode is 50–60 μl mg^{-1}. The working electrodes were fabricated by uniformly blending TiN@C powders (70 wt.%), Super P carbon black (20 wt.%), and polyvinylidene fluoride (PVDF, 10 wt%) in N-methyl-2-pyrrolidinone (NMP) solvent. Then the resultant slurry was pasted onto a piece of copper foil, and dried under vacuum at 120 °C for 12 h. The mass loading of TiN@C is ~1.5 mg cm^{-2}.

2.4. Electrochemical measurements

Galvanostatic charge–discharge and galvanostatic intermittent titration technique (GITT) measurements were conducted by a Land CT3001A cell tester in the potential range of 0.01–3.0 V to 0.1–3.0 A g^{-1}. Cyclic Voltammetries (CV) at 0.2–10 mV s^{-1} in the potential range of 0.01–3.0 V and electrochemical impedance spectroscopies (EIS) data with a frequency ranging from 10^5 to 10^{-2} Hz were collected by an electrochemical workstation (CHI760e, Shanghai CH Instrument Company).

3. Results and discussion

3.1. Materials synthesis and characterizations

TiN@C samples were synthesized by a simple molten salt synthesis method; a detailed schematic diagram of the preparation process is presented in figure 1. The formation mechanism of TiN@C could be ascribed to the disproportionation reaction of Ti(II)-ions on the g-C_3N_4 surface, as elucidated in nanosized TiC [18]. As the reaction temperature is raised to 352 °C, (Li,K)Cl salts melt into liquid. It is feasible for melamine to decompose into carbon nitride (g-C_3N_4) through the thermal condensation reaction at 450 °C (The morphology of g-C_3N_4 is shown in figure 1) [19]. As is well known, some oxidizing impurities including H_2O and O_2 could not be removed completely in (Li,K)Cl molten salts. At a high temperature, (Li,K)Cl would react with H_2O to generate gaseous HCl. It is possible for HCl to attack metallic Ti to produce Ti(II)-ions and Ti(III)-ions [18]. Then Ti(II)-ions would diffuse towards the g-C_3N_4 surface, which serves as the template to promote the disproportionation reaction into atomic Ti and Ti(III)-ions. Due to the lower Gibbs energy of TiN than TiC, TiN could be *in-situ* synthesized between the chemical reaction of atomic Ti and N on g-C_3N_4 surface, whereas the residual amorphous carbon would act as the skeleton to support the formed TiN nanoparticles. Additionally, the generated Ti(III)-ions can further react with metallic Ti to form Ti(II)-ions until the thorough consumption of metallic Ti powders. Hence, the specific reaction procedures can be described using the following equations:

$$10\mathrm{Ti} + 10\mathrm{HCl} = 2\mathrm{Ti\,(II)\,Cl_2} + 2\mathrm{Ti\,(III)\,Cl_3} + 5\mathrm{H_2} \quad (1)$$

$$12\mathrm{Ti\,(II)} + g\text{-}\mathrm{C_3N_4} = 4\mathrm{TiN} + 8\mathrm{Ti\,(III)} + 3\mathrm{C} \quad (2)$$

$$2Ti\,(\mathrm{III}) + Ti = 3Ti\,(\mathrm{II})\,. \quad (3)$$

Figure 2(a) shows the XRD patterns of TiN@C heated at 500 °C, 600 °C, 700 °C, 800 °C, and 900 °C holding for 3 h in molten (Li,K)Cl salts under Ar atomosphere, named as TiN@C-500, TiN@C-600, TiN@C-700, TiN@C-800, and TiN@C-900, respectively. All the main diffraction peaks are well indexed to TiN with *Fm-3 m* space group (PDF#38-1420). There are some residual g-C_3N_4 impurities in samples sintered at 500 °C–700 °C, possibly related to its incomplete decomposition during the synthesis process. Meanwhile, compared with samples prepared at 700 °C–900 °C, TiN@C-500 and TiN@C-600 show poorer crystallinity, which is probably related to the lower sintering temperatures. As shown in figure 2(b), the XRD Rietveld refinement result illustrates the excellent crystallinity of TiN@C-700. The schematic diagram of TiN in the figure 2(c) exhibits the large interstices between Ti and N atoms, which could accommodate the fast Li-ions migration and promote the electrochemical reaction. Figure 2 displays the XPS full spectrum of TiN@C-700, confirming

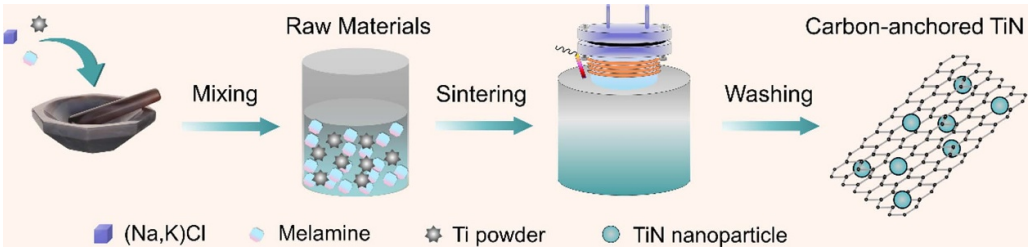

Figure 1. Schematic illustration of of carbon-anchored TiN nanoparticles via a molten salt synthesis strategy.

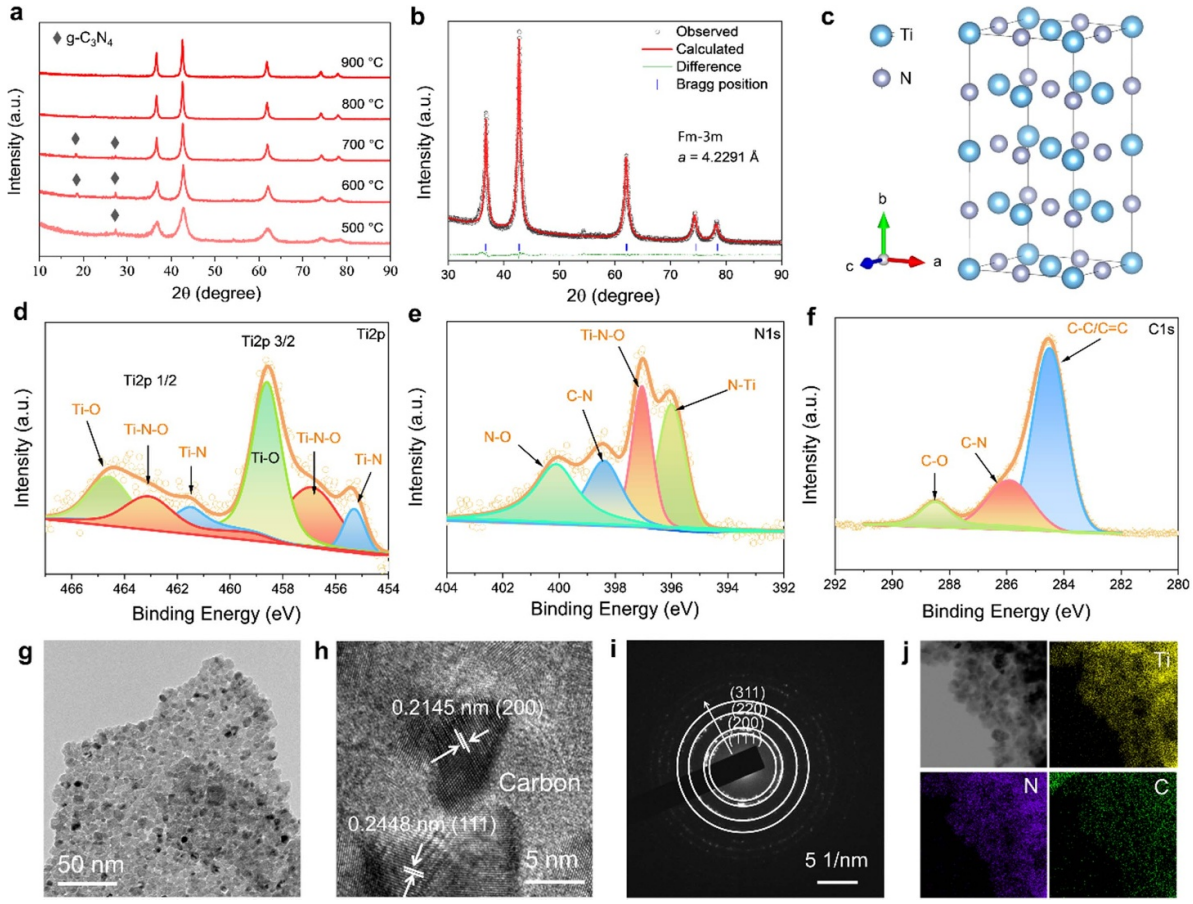

Figure 2. Structure and morphology characterizations. (a) XRD patterns of TiN@C synthesized at different temperatures; (b) rietveld refinement of XRD pattern for TiN@C-700; (c) schematic diagram of cubic TiN; (d)–(f) XPS spectra of Ti 2p (d), N 1s (e), C 1s (f) and (g) TEM image, (h) HRTEM image, (i) SAED pattern, and (j) EDS mapping images of Ti, C and N elements for TiN@C-700.

the presence of Ti, C, N, and O elements. Existence of O element may be attributed to the surface oxygen adsorption at air or/and slight oxidization of TiN during the synthesis process in liquid molten salt environment. As shown in figure 2(d), three pairs of fitting peaks appeared at 464.6 and 458.6 eV, 463.1 and 456.95 eV, 461.5 and 455.3 eV in Ti2p 1/2 and Ti2p 3/2 spectra, corresponding to Ti–O, Ti–N–O, and Ti–N bonds, respectively [15]. Four fitting peaks at 400.05, 398.4, 397.05, and 396.0 eV in N1s spectrum (figure 2(e)) are assigned to N–O, C–N, Ti–N–O, and N–Ti bonds, respectively [16]. It is also evident to observe three fitting peaks at 288.5, 285.9, and 284.5 eV in C 1s spectrum (figure 2(f)), indexed to C–O, C–N, and C–C (C=C) bonds, respectively [16]. These aforementioned results also clearly verified the formation of TiN@C. The SEM image of TiN@C-700 (figure 3) shows that well-distributed TiN nanoparticles were coated onto plate-like carbon, leading to a high electrical conductivity. TEM image in figure 2(g) further suggests the uniform distribution of spherical TiN nanoparticles anchored onto carbon, with an average particle size of 5 nm observed. The presence of plate-like carbon is possibly derived from the remanent amorphous carbon after the decomposition of melamine at a high temperature.

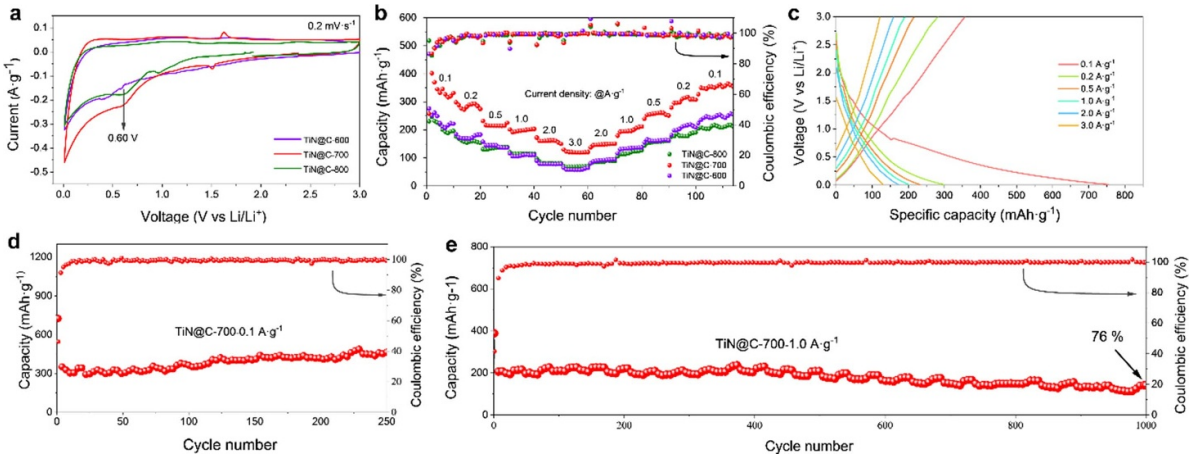

Figure 3. Electrochemical performances of carbon-anchored TiN nanoparticles. (a), (b) Initial CV curves at 0.2 mV s^{-1} (a) and rate capabilities (b) of TiN@C-600, TiN@C-700, and TiN@C-800; (c)–(e) First charge–discharge curves at 0.1 $\sim$ 3.0 A g^{-1} (c) and cycling properties (d), (e) at 0.1 and 1.0 A g^{-1} of TiN@C-700.

HRTEM image in figure 2(h) also exhibits the microstructure of nanosized TiN interconnected by amorphous carbon. Clear lattice distances of 0.2145 and 0.2448 nm are assigned to (200) and (111) crystallographic planes of TiN (figure 2(h)). SAED in figure 2(i) further confirms the cubic microstructure of TiN. EDS mapping images (figure 2(j)) manifest that Ti, N, and C elements were distributed uniformly in TiN@C.

3.2. Electrochemical performances

Electrochemical performances of TiN@C were evaluated by Li-ions half cells in the potential range of 0.01–3.0 V at room temperature. Figure 3(a) displays the initial CV curves of TiN@C obtained at 600 °C–800 °C at 0.2 mV s^{-1}. It is notable that TiN@C-700 exhibits the largest curve integral area compared to that of TiN@C-600 and TiN@C-800, suggesting the highest capacities. An irreversible cathodic peak appeared at approximately 0.60 V during the first discharging process, which is probably assigned to the formation of solid electrolyte interface (SEI) film and irreversible chemical reactions between titanium oxides on TiN surface and electrolyte [20]. CV profiles of TiN@C-700 are overlapped well, manifesting a high electrochemical reversibility of TiN@C-700 (figure 4). Figure 3(b) exhibits the rate properties of TiN@C-600, TiN@C-700, and TiN@C-800 at 0.1–3.0 A g^{-1}. Notably, TiN@C-700 displayed more highlighted discharge capacities than that of TiN@C-600 and TiN@C-800, with a reversible discharge capacity of 343.4, 285.3, 217.8, 198.4, 160.7, and 121.2 mAh g^{-1} obtained at 0.1, 0.2, 0.5, 1.0, 2.0, and 3.0 A g^{-1}, respectively. The impressive capacities of TiN@C-700 than that of TiN@C-800 may be attributed to its lower synthesis temperature, with larger specific surface areas and more achieved electroactive sites. The high specific surface areas could promote and advance the electrochemical reaction of TiN with Li-ions during the charge–discharge process. Meanwhile, to some extent, the residual g-C_3N_4 could also enhance the structure stability and prevent the agglomeration of TiN nanoparticles during cycling [21]. The poorer crystallinity of TiN@C-600 is possibly the main reason that results in the lower capacities compared to TiN@C-700. When the current density returns to 0.1 A g^{-1}, the reversible capacity of TiN@C-700 can recover its initial value of 349.6 mAh g^{-1}, indicating its excellent structural reversibility. The initial discharge and charge capacities of TiN@C-700 are 754.3 and 356.5 mAh g^{-1}, respectively, with a coulombic efficiency (CE) of 47.3 %. Such a low CE may be correlated with the formation of incomplete SEI film on the TiN@C surface during the first cycling process, which is relevant to the microstructure of nanosized TiN anchored onto carbon. This behavior is also consistent with the CV curves shown in figure 3(a). After the initial several cycles, CE of TiN@C maintains $\sim$100 %, clarifying the enhanced electrolyte filtration accompanied by the gradually stable growth of SEI film. Additionally, such an impressive rate capability of TiN@C-700 is possibly attributed to the uniform distribution of TiN nanoparticles with abundant electrochemical sites exposed for Li-ions storage. From the first charge–discharge curves of TiN@C-700 at 0.1–3.0 A g^{-1} in figure 3(c), it is notable that more than 70% discharge capacities were shown below $\sim$0.80 V, further illustrating that TiN@C is a representative anode material for LIBs.

To further investigate the cyclabilities of TiN@C-700, cycling properties were tested at 0.1 and 1.0 A g^{-1} (figures 3(d) and (e)). It is worth noting that TiN@C-700 released a capacity of 381.5 mAh g^{-1} at 0.1 A g^{-1} after 250 cycles without capacity decay. For the initial 10 cycles, the discharge capacity of TiN@C decreases gradually, possibly associated with the formation and gradual growth of the stable SEI film. Interestingly, there is a clear upward trend for reversible capacities of TiN@C in the subsequent cycles. This result may be related to the constant activation and enhanced electrolyte filtration for TiN nanopartciles during cycling, accompanied by the

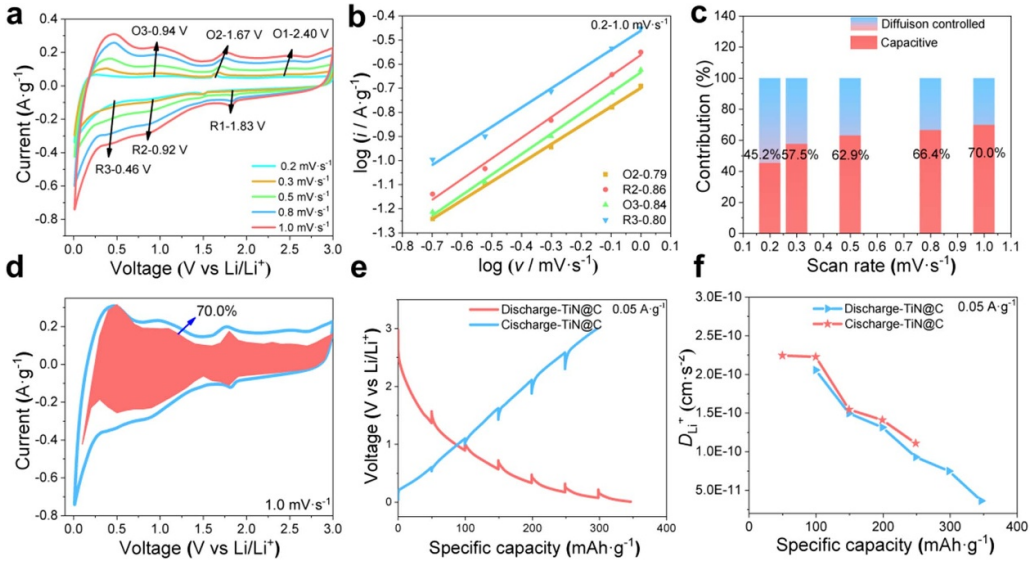

Figure 4. Electrochemical reaction kinetics of TiN@C-700. (a) CV curves at 0.2–1.0 mV s^{-1}; (b) *b* values calculated from cathodic and anodic peak currents; (c) capacitive and diffusion contribution ratios at 0.2–1.0 mV s^{-1}; (d) calculated capacitive contribution at 1.0 mV s^{-1}; (e), (f) GITT profiles and corresponding Li-ions diffusion coefficients during the charge and discharge process at 0.05 A g^{-1}.

exposure of substantial new electroactive sites [22]. Moreover, with the continuous cycling, the drastically enhanced charge transfer kinetics in nanosized TiN would enable new electrochemical reactions which does not exist in bulk materials, and the effect of nanocrystallization after the long-term cycling at 0.1 A g^{-1} could also improve the specific surface areas of active materials, resulting in the participation in charge transfer of inactive domains [23]. Simultaneously, the domain size of active materials could be reduced during cycling at 0.1 A g^{-1}, leading to the generation of new electroactive sites. As depicted in figure 3(e), TiN@C-700 showed a reversible capacity of 141.5 mAh g^{-1} at 1.0 A g^{-1} after 1000 cycles, with the capacity retention of 76% obtained. This result also demonstrates the outstanding long-term cycling stability of TiN@C at large current densities. Such a remarkable cycling stability of TiN@C may mainly originate from the robust structural support of carbon towards TiN nanoparticles, which is conducive to improve the overall electrical conductivity and structural durability. It is beneficial to promoting the electrons and Li-ions migration in nanosized TiN, contributing to a rapid electrochemical reaction kinetics. Furthermore, the prominent structural stability of TiN@C could not only accommodate the strain variation, but restrain the aggregation and pulverization of nanosized TiN during cycling. Furthermore, to some extent, the existence of g-C_3N_4 support could further prevent the agglomeration and/or structural collapse and/or volume variation of TiN during cycling, with the superior rate and cycling capabilities achieved for TiN@C-700. SEM and TEM images in figure S5 also show the intact preservation of nanosized TiN with excellent crystallinity after 1000 cycles at 1.0 A g^{-1}, further suggesting the good structural stability and reversibility.

To study the electrochemical reaction kinetics, CV curves of TiN@C-700 at 0.2–1.0 mV s^{-1} were tested and are shown in figure 4(a). Three pairs of redox peaks were observed at 2.40/1.83 V, 1.67/0.92 V, and 0.94/0.46 V, relevant to reversible electrochemical reactions of TiN and surface Ti-based oxides with Li-ions during the lithiation/delithiation process [15]. *b* value could be calculated by the following equation [24].

$$i = av^b \tag{4}$$

where *i* and *v* denote the peak current (A) and scan rate (mV s^{-1}), respectively. *a* and *b* are constants, where *b* values of 1.0 and 0.5 represent a completely capacitive or diffusion-dominated process, respectively. For this TiN@C-700, *b* value is approximately 0.80 (figure 4(b)), illustrating that the main Li-ions storage behavior of TiN@C is capacitive. The specific capacitive contribution at 0.2–1.0 mV s^{-1} could be determined by equation (5) [24]:

$$i = k_1 v + k_2 v^{1/2} \tag{5}$$

where $k_1 v$ and $k_2 v^{1/2}$ are capacitive and diffusive-controlled contributions, respectively. As shown in figure 4(c), the capacitive contribution ratio increases with scan rate, accompanied by high capacitive contributions ratio at large scan rates, thereinto the ~70% capacitive contribution ratio could be achieved at 1.0 mV s^{-1} (figure 4(d)). To evaluate the charge–discharge kinetics of TiN@C-700, Li-ions diffusion coefficients were obtained according to GITT method using equation (6) [25]:

$$D = \frac{4}{\pi\tau}\left(\frac{n_m V_m}{S}\right)^2\left(\frac{\Delta E_s}{\Delta E_t}\right)^2 \tag{6}$$

where τ is the relaxation time of constant current pulse, n_m, V_m, and *S* represent moles, mole volume, and electrode-electrolyte contact areas of active materials. ΔE_S and ΔE_t denote the potential change caused by the current pulse and

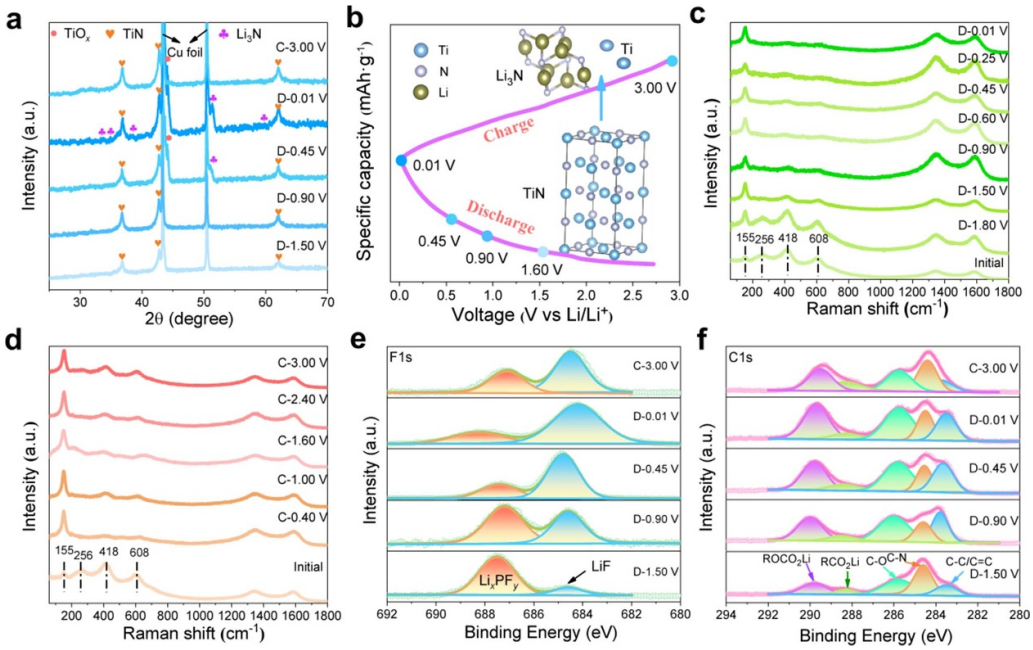

Figure 5. (a), (b) *Ex-situ* XRD (a) and corresponding selected voltage distribution and structure variation schematic diagrams (b) of TiN@C-700 during the charge–discharge process at 0.1 A g^{-1}. (c), (d) *Ex-situ* Raman spectra, (e), (f) *ex-situ* XPS spectra of F 1s (e) and C 1s (f).

galvanostatic charge and discharge, respectively. As presented in figures 4(e) and (f), $D_{Li}{}^{+}$ values of TiN@C-700 have ranged from 3.65 × 10^{-11} to 2.25 × 10^{-10} cm s^{-2}, which are comparable to as-reported anode materials such as perovskite-type $SrVO_3$ [26], vanadium nitride/N-doped carbon composite [27], V_2CT_z MXene [28], 3D hollow porous V_2O_5 [5], SiO_2/TiO_2 [29] (table S1).

3.3. Structural evolution and reaction mechanisms

Ex-situ XRD, Raman, and XPS measurements were carried out to study the structural evolution and Li-ions storage mechanism of TiN@C. Figures 5(a) and (b) exhibit *ex-situ* XRD patterns and corresponding selected voltage distribution of TiN@C-700 during the Li-ions insertion/extraction process. With the decline of lithiation voltage to 1.50 and 0.90 V, it is clear that the main phases of TiN@C are still TiN. However, as the discharge voltage was further decreased to 0.45 and 0.01 V, two new phases of Li_3N and titanium oxides have appeared in TiN@C-700, except with more contents obtained at 0.01 V. These results illustrated that the electrochemical conversion reaction between TiN and Li-ions have occurred below 0.90 V during the charge–discharge process, leading to the formation of Li_3N and amorphous Ti. The SAED pattern and HRTEM image in figure S6 further proved the generation of Ti and Li_3N at the discharge voltage of 0.01 V. The detailed schematic illustration of the chemical conversion reaction of TiN into Ti and Li_3N is shown in the figure 5(b) inset. However, amorphous Ti under an unstable state could be oxidized easily at room temperature, resulting in the detection of titanium oxides. After charged to 3.0 V again, the sole TiN phases were detected distinctively, further demonstrating the excellent reversibility of the electrochemical conversion reaction.

Figure 5 c shows the Raman spectra of TiN@C-700 during the Li-ions insertion and extraction process at 0.01–3.0 V. It is interesting to observe two representative peaks at 1345 and 1590 cm^{-1}, corresponding to D and G bands of residual carbon in TiN@C samples, respectively. It is known that the position, intensity, and shape of D and G bands are strongly affected by the uptake and adsorption of Li-ions into the carbon-based host [30]. However, during the whole lithiation/delithiation process at 0.01–3.0 V, there is almost no variation for the I_D/I_G ratio (1.09–1.10), peak position, and shape of D and G bands. This result suggests that Li-ions de-/intercalation into amorphous carbon is not the main capacity contribution source in TiN@C samples. Only small amount of Li-ions were embedded into carbon layers, resulting in the generation of some capacities in the form of electric double layer capacitance. Additionally, it is evident to observe four distinctive peaks at 155, 256, 418, and 608 cm^{-1}, which are typical characteristics of TiN [31]. During the discharge process to 0.01 V, the Raman peaks at 256, 418, and 608 cm^{-1} disappeared gradually. This result is possibly related to the formation of SEI film and the electrochemical conversion reaction between TiN and Li-ions, which is possibly conducive to the generation of amorphous Ti and Li_3N. Notably, with the elevated charge voltage to 3.0 V, all the representative Raman peaks of TiN appeared distinctly, further illustrating the remarkable reversibility of electrochemical reaction. These results are in good accordance with XRD patterns shown in figures 5(a) and (b).

Ex-situ XPS spectra of TiN@C-700 (figure S7) further elucidated the electrochemical conversion reaction between TiN with Li-ions during the charge–discharge procedure, which has contributed to the formation of Li_3N and Ti. To further study the formation and growth of SEI film on the TiN surface, corresponding F 1s and O 1s spectra were also collected (figures 5(e) and (f)). The surface of SEI layer generated in traditional electrolyte is mainly composed of organic LiF and RCH_2OCO_2Li [32]. As shown in figure 5(e), it is notable that the peak intensity of Li-F bond increased gradually and almost remained unchangeable at 0.45 V during the discharging process. This result manifests that SEI film has reached the stable formation upon 0.45 V, in good accordance with the first CV curves shown in figure 3(a). Moreover, as presented in the C1s spectra (figure 5(f)), the typical peaks of $ROCO_2Li$ and RCO_2Li approached to the stable states at 0.90–0.45 V, further clarifying the generation of stable SEI layer on the TiN surface. Additionally, after charged to 3.0 V, there is almost no composition variation for F1s and C1s spectra, which further confirm the irreversible formation of SEI film on the TiN@C surface. Based on these experimental results, it is definitely speculated that there is a reversible chemical conversion reaction between TiN and Li-ions ($TiN + 3e^- + 3Li^+ = Ti + Li_3N$) during the cycling process, which contributed to the majority of Li-ions storage capacities.

4. Conclusions

In summary, a simple and low-cost synthesis route of carbon-anchored TiN nanoparticles (TiN@C) was developed by the molten salt synthesis method. TiN@C has displayed prominent electrochemical performances as a high-rate anode for fast charging-discharging LIBs, which could show a reversible capacity of ~381.5 mAh g^{-1} at 0.1 A g^{-1} after 250 cycles and ~141.5 mAh g^{-1} at 1.0 A g^{-1} after 1000 cycles, respectively. Such remarkable rate capabilities of TiN@C could be derived from its robust microstructure of TiN nanoparticles dispersed onto the carbon support. Simultaneously, nanosized TiN in ~5 nm particle size possessed large specific surface areas, accompanied by abundant electroactive sites generated for Li-ions storage. Li-ions storage mechanism of TiN@C is a conversion reaction, along with the reversible electrochemical reaction of $TiN + 3e^- + 3Li^+ = Ti + Li_3N$ during the Li-ions insertion and extraction process. These findings highlight the feasibility and superiority of this preparation method for TiN as a durable high-rate anode for LIBs.

Acknowledgments

This work is supported by National Natural Science Foundation of China (No. 51671204), Guangdong Basic and Applied Basic Research Foundation, China (No. 2019A1515110825).

Author contributions

Ruijia Liu: experiments, data processing and analyses, and writing original manuscript. Na Li: investigations, and assisted experiments. Enyue Zhao*: investigations, review & editing, and data analyses. Jinkui Zhao: review & editing. Wenjun Wang: characterizations and data analyses. Lingxu Yang: characterizations and data analyses. Huijun Liu*: review & editing, and characterizations. Chaoliu Zeng*: supervision and funding acquisition.

Conflict of interest

No potential conflict of interest was reported by the authors.

ORCID iD

Enyue Zhao https://orcid.org/0000-0003-4170-7427

References

[1] Ben L, Zhou J, Ji H, Yu H, Zhao W and Huang X 2021 Si nanoparticles seeded in carbon-coated Sn nanowires as an anode for high-energy and high-rate lithium-ion batteries *Mater. Futures* **1** 015101
[2] Zhou G M, Li F and Cheng H M 2014 Progress in flexible lithium batteries and future prospects *Energy Environ. Sci.* **7** 1307
[3] Goodenough J B and Park K S The Li-ion rechargeable battery: a perspective 2013 *J. Am. Chem. Soc.* **135** 1167
[4] Chen Z, Liu Y, Zhang Y, Shen F, Yang G, Wang L, Zhang X, He Y, Luo L and Deng S 2018 Ultrafine layered graphite as an anode material for lithium ion batteries *Mater. Lett.* **229** 134
[5] Yan B, Li X, Fu X, Zhang L, Bai Z and Yang X 2020 An elaborate insight of lithiation behavior of V_2O_5 anode *Nano Energy* **78** 105233
[6] Jiang L, Qu Y, Ren Z, Yu P, Zhao D, Zhou W, Wang L and Fu H 2015 *In situ* carbon-coated yolk-shell V_2O_3 microspheres for lithium-ion batteries *ACS Appl. Mater. Interfaces* **7** 1595
[7] Bai J, Zhao B, Lin S, Li K, Zhou J, Dai J, Zhu X and Sun Y 2020 Construction of hierarchical V_4C_3-MXene/MoS_2/C nanohybrids for high rate lithium-ion batteries *Nanoscale* **12** 1144
[8] Kong F, He X, Liu Q, Qi X, Zheng Y, Wang R and Bai Y 2018 Effect of Ti_3AlC_2 precursor on the electrochemical properties of the resulting MXene Ti_3C_2 for Li-ion batteries *Ceram. Int.* **44** 11591
[9] Zhou J, Lin S, Huang Y, Tong P, Zhao B, Zhu X and Sun Y 2019 Synthesis and lithium ion storage performance of two-dimensional V_4C_3 MXene *Chem. Eng. J.* **373** 203
[10] Chen S, Yang X Y, Zhang J, Ma J P, Meng Y Q, Tao K J, Li F and Geng J X 2021 Aluminum-lithium alloy as a stable and reversible anode for lithium batteries *Electrochim. Acta* **368** 137626
[11] Zhong Y, Xia X, Shi F, Zhan J, Tu J and Fan H J 2016 Transition metal carbides and nitrides in energy storage and conversion *Adv. Sci.* **3** 1500286
[12] Balogun M-S, Huang Y, Qiu W, Yang H, Ji H and Tong Y 2017 Updates on the development of nanostructured transition metal nitrides for electrochemical energy storage and water splitting *Mater. Today* **20** 425
[13] Liu R J, Yang L X, Wang W J, Liu H J and Zeng C L 2022 Molten salt disproportionation synthesis of nanosized VN wrapped onto carbon fibers with enhanced lithium-ion storage capabilities *J. Alloys Compd.* **919** 165796

[14] Wang J, Yang C, Wu J, Zhang L and Wei M 2019 Facile synthesis of VN hollow spheres as an anode for lithium-ion battery *J. Electroanal. Chem.* **848** 113360
[15] Balogun M-S, Yu M, Li C, Zhai T, Liu Y, Lu X and Tong Y 2014 Facile synthesis of titanium nitride nanowires on carbon fabric for flexible and high-rate lithium ion batteries *J. Mater. Chem.* A **2** 10825
[16] Xiu Z, Kim D, Alfaruqi M H, Gim J, Song J, Kim S, Duong P T, Baboo J P, Mathewa V and Kim J 2016 Porous TiN nanoparticles embedded in a N-doped carbon composite derived from metal-organic frameworks as a superior anode in lithium-ion batteries *J. Mater. Chem.* A **4** 4706
[17] Dash B B and Rav S 2016 Sign reversal of magnetization in Mn substituted $SmCrO_3$ *J. Magn. Magn. Mater.* **405** 209
[18] Yang L, Wang Y, Liu R, Liu H, Zhang X, Zeng C and Fu C 2020 *In-situ* synthesis of nanocrystalline TiC powders, nanorods, and nanosheets in molten salt by disproportionation reaction of Ti(II) species *J. Mater. Sci. Technol.* **37** 173
[19] Tian L, Li J, Liang F, Wang J, Li S, Zhang H and Zhang S 2018 Molten salt synthesis of tetragonal carbon nitride hollow tubes and their application for removal of pollutants from wastewater *Appl. Catal.* B **225** 307
[20] Cheng H, Garcia-Araez N and Hector A L 2020 Synthesis of vanadium nitride-hard carbon composites from cellulose and their performance for sodium-ion batteries *ACS Appl. Energy Mater.* **3** 4286
[21] Liu K, Man J, Cui J, Zhang H, Li T, Yang J, Wen Z and Sun J 2019 $Li_4Ti_5O_{12}$/g-C_3N_4 composite with an improved lithium storage capability *Mater. Lett.* **234** 117
[22] Kang Y, Zhang Y-H, Shi Q, Shi H, Xue D and Shi F N 2020 Highly efficient Co_3O_4/CeO_2 heterostructure as anode for lithium-ion batteries *J. Colloid Interface Sci.* **585** 705
[23] Kim H, Choi W, Yoon J, Um J, HLee W, Kim J, Cabana J and Yoon W-S 2020 Exploring anomalous charge storage in anode materials for next generation Li rechargeable batteries *Chem. Rev.* **120** 6934
[24] Wei S, Wang C, Chen S, Zhang P, Zhu K, Wu C, Song P, Wen W and Song L 2020 Dial the mechanism switch of VN from conversion to intercalation toward long cycling sodium-ion battery *Adv. Energy Mater.* **10** 1903712
[25] Liu Y *et al* 2020 In-situ electrochemically activated surface vanadium valence in V_2C MXene to achieve high capacity and superior rate performance for Zn-ion batteries *Adv. Funct. Mater.* **31** 2008033
[26] Li X, Lin Z, Jin N, Yang X, Du Y, Lei L, Rozier P, Simon P and Liu Y 2021 Perovskite-type $SrVO_3$ as high-performance anode materials for lithium-ion batteries *Adv. Mater.* 2107262
[27] Tang C, Tao H, Liu X and Yang X 2022 VN quantum dots embedded in N-doped carbon for high performance lithium storage *Energy Fuel* **36** 1043
[28] Ming F, Liang H, Zhang W, Ming J, Lei Y, Emwas A-H and Alshareef H N 2019 Porous MXenes enable high performance potassium ion capacitors *Nano Energy* **62** 853
[29] Li R, Xiao W, Miao C, Fang R, Wang Z and Zhang M 2019 Sphere-like SnO_2/TiO_2 composites as high-performance anodes for lithium ion batteries *Ceram. Int.* **45** 13530
[30] Zhang C, Liu X, Li Z, Zhang C, Chen Z, Pan D and Wu M 2021 Nitrogen-doped accordion-like soft carbon anodes with exposed hierarchical pores for advanced potassium-ion hybrid capacitors *Adv. Funct. Mater.* **31** 2101470
[31] Djire A, Bos A, Liu J, Zhang H, Miller E M and Neale N R 2019 Pseudocapacitive storage in nanolayered Ti_2NT_x MXene using Mg-ion electrolyte *ACS Appl. Nano Mater.* **2** 2785
[32] Chen J *et al* 2020 Electrolyte design for LiF-rich solid-electrolyte interfaces to enable high-performance microsized alloy anodes for batteries *Nat. Energy* **5** 386